

<https://doi.org/10.1016/j.jnucmat.2021.153244>

Dislocation Loops in Proton Irradiated Uranium-Nitrogen-Oxygen System

Pengyuan Xiu^{a,b*}, Miaomiao Jin^c, Kaustubh Bawane^a, Beata Tyburska-Püschel^d, Brian J. Jaques^e, Kevin G. Field^b, Jeffrey J. Giglio^a, Lingfeng He^{a*}

^a Idaho National Laboratory, Idaho Falls, ID 83415, USA

^b Department of Nuclear Engineering and Radiological Sciences, University of Michigan, Ann Arbor, MI 48109, USA

^c Department of Nuclear Engineering, The Pennsylvania State University, University Park, PA 16802, USA

^d Dutch Institute for Fundamental Energy Research, 5612 AJ Eindhoven, The Netherlands

^e Micron School of Materials Science and Engineering, Boise State University, Boise, ID 83725, USA

Abstract

In this study, we investigated the dislocation loop types formed in the proton-irradiated uranium-nitrogen-oxygen (U-N-O) system, which involves uranium mononitride (UN), uranium sesquinitride (α -U₂N₃), and uranium dioxide (UO₂) phases. The dislocation loop formation is examined using specimens irradiated at 400°C and 710°C. Based on the detailed transmission-based electron microscopy characterization with i) the morphology-based on-zone and ii) the invisibility-criterion based two-beam condition imaging techniques, only a single type of dislocation loop in each phase is found: $a/2\langle 110 \rangle$, $a/2\langle 111 \rangle$, or $a/3\langle 111 \rangle$ dislocation loops in UN, α -U₂N₃, and UO₂ phases, respectively. Molecular statics calculations for the formation energy of perfect and faulted dislocation loops in UN phases indicate a critical loop size of ~ 6 nm, above which perfect loops are energetically favorable. This could explain the absence of faulted loops in the experimental observation of the irradiated UN phase at two temperatures. This work will enhance the understanding of irradiation induced microstructural evolution for uranium nitrides as advanced nuclear fuels for the next-generation nuclear reactors.

Keywords: radiation effects; dislocation loops; uranium nitride; nuclear fuels

*Corresponding authors: Pengyuan Xiu, xiupy@umich.edu

Lingfeng He, lingfeng.he@inl.gov

1
2
3
4 **1. Introduction**
5

6
7 2 Uranium mononitride (UN) has been considered a candidate fuel material for advanced nuclear
8
9 3 systems including liquid metal-cooled fast reactors, high-temperature gas-cooled reactors, and
10
11 4 light water reactors [1–10] due to its multiple advantages [3]: (i) higher fissile density (40% more
12
13 5 uranium in UN than in uranium dioxide, UO₂), (ii) higher thermal conductivity, (iii) easier
14
15 6 preprocessing, (iv) good irradiation stability and chemical compatibility with most potential
16
17 7 cladding materials, and (v) longer fuel cycle time.
18
19
20
21

22 8 The phase and dislocation loop evolution in the uranium-nitrogen-oxygen system under proton
23
24 9 irradiation has been recently studied [9]. Irradiation can enhance the oxidation of UN, which
25
26 10 creates two fully coherent phases, alpha uranium sesquinitride (α -U₂N₃) and UO₂ [9]. UN has a
27
28 11 rocksalt crystal structure, α -U₂N₃ has a body-center-cubic (BCC) based Mn₂O₃-type crystal
29
30 12 structure [11], and UO₂ has a fluorite crystal structure [12]. The dislocation loop size was found
31
32 13 three times larger in the two nitride phases, UN and α -U₂N₃, than in UO₂, while the number density
33
34 14 was one order of magnitude higher in UO₂ than in the nitride phases [9].
35
36
37
38
39

40 15 However, the characteristics of dislocation loops such as the Burgers vector and habit plane in
41
42 16 the abovementioned three phases under proton irradiation have not been studied in detail. Although
43
44 17 the defects in actinide nitrides are rarely investigated, zirconium nitride (ZrN) was used as a
45
46 18 common non-radioactive surrogate for UN to study the radiation effects [13,14] because ZrN
47
48 19 shares the same crystal structure with UN. Yang et al. [13] used the high-resolution transmission
49
50 20 electron microscopy (HRTEM) technique to show that vacancy-type pyramidal dislocation loops
51
52 21 formed in ZrN under proton irradiation to 0.75 dpa at 800°C, while faulted dislocation loops were
53
54 22 not observed using rel-rod dark field imaging technique. Bao et al. [15] showed $a/2\langle 110 \rangle$
55
56 23 dislocation loop formation in the polycrystalline ZrN under gold irradiation. In another study, Jiao
57
58
59
60
61
62
63
64
65

1
2
3
4 24 et al. [14] observed both interstitial- and vacancy-types of dislocation loops using HRTEM in iron
5
6 25 irradiated nanocrystalline ZrN films.
7
8

9
10 26 Dislocation loop analysis in the traditional nuclear fuel UO_2 under heavy ion irradiation (using
11
12 27 Cs, Kr, or Xe ions) has been studied for decades. These studies [16–19] showed the exclusive
13
14 28 existence of $a/2\langle 110 \rangle$ perfect type of dislocation loops in heavy ion irradiated UO_2 , while very
15
16 29 limited neutron or electron irradiation experimental data [20] showed the existence of only
17
18 30 $a/3\langle 111 \rangle$ faulted dislocation loops. The disparity is likely a result of cascade size difference
19
20 31 induced by heavy ions with varying mass and charge; this hypothesis may be validated using light-
21
22 32 ion irradiation, such as protons. In addition, molecular dynamics (MD) simulation studies of UO_2
23
24 33 [21–23] indicated that interstitial clusters may initially aggregate to form small $a/3\langle 111 \rangle$ faulted
25
26 34 dislocation loops, which is a more stable configuration compared to $a/2\langle 110 \rangle$ perfect dislocation
27
28 35 loops. With increasing size, unfaulting can occur due to the increasing stacking fault energy, which
29
30 36 has been reported by experiments and simulations in irradiated face-center-cubic (FCC) materials
31
32 37 [24–32]. Besides the direct investigation of irradiated UO_2 , dislocation loop analysis of ion
33
34 38 irradiated thorium dioxide (ThO_2), sharing the same crystal structure of UO_2 , has also been studied.
35
36 39 Mixed data have been reported [33–35] in irradiated ThO_2 with the formation of $a/2\langle 110 \rangle$ and/or
37
38 40 $a/3\langle 111 \rangle$ type of dislocation loops due to different irradiation conditions such as ion species,
39
40 41 temperature, and damage level.
41
42

43
44 42 To analyze proton-irradiation-induced dislocation loops in the U-N-O system (three phases:
45
46 43 UN and $\alpha\text{-U}_2\text{N}_3$, and UO_2), we used developed scanning/transmission electron microscopy
47
48 44 (S/TEM) techniques with the aid of several methods for classification of loop types based on
49
50 45 observed contrast and morphology [36–38]. The on-zone STEM technique coupled with simulated
51
52 46 morphology maps has been recently developed and applied to characterize dislocation loop
53
54
55
56
57
58
59
60
61
62
63
64
65

1
2
3
4 47 formation in irradiated FCC [38] and BCC [36,37] alloys. It has been demonstrated that dislocation
5
6 48 loops of various types [29,38–40] in these alloys can be unambiguously identified, given the
7
8
9 49 correct orientation is used, based on their projection morphology when the dislocation loop size is
10
11 50 above a given size threshold, typically around 5-10 nm for most STEM instruments and imaging
12
13 51 conditions. In addition, STEM imaging has multiple advantages of (i) suppressing background
14
15 52 contrast to improve signal-to-noise ratio [41], (ii) exhibiting all dislocation loops within the TEM
16
17 53 specimen when the on-zone condition is satisfied [42], and (iii) the applicability of some common
18
19 54 conventional transmission electron microscopy (CTEM) techniques for dislocation loop analysis
20
21 55 such as the two-beam condition imaging that utilizes the $\vec{g} \cdot \vec{b}$ invisibility criterion [43,44].
22
23 56 Furthermore, to gain a fundamental understanding towards the observed dislocation loop types,
24
25 57 MD simulations are applied to reveal the energetically favorable atomic configuration and
26
27 58 calculate the size-dependent formation energy of dislocation loops in irradiated UN.
28
29
30
31
32
33

34 59 **2. Methods**

35 60 **2.1 Proton Irradiation**

36
37 61 The UN-5wt.%UO₂ samples were irradiated with 2 MeV proton ions to reach the total fluence
38
39 62 of 8×10^{18} ions/cm² at 400°C and 710°C, respectively [9]. The proton flux was maintained at
40
41 63 5.2×10^{13} ions/(cm²s) for the low-temperature irradiation and 7.5×10^{13} ions/(cm²s) for the high-
42
43 64 temperature irradiation, resulting in a damage rate of 4.1×10^{-6} and 5.9×10^{-6} dpa/s, respectively for
44
45 65 UN. The Stopping and Range of Ions in Matter (SRIM) 2013 code in “Detailed Calculation with
46
47 66 Full Damage Cascades” mode [45] was used to calculate the proton-irradiation damage with the
48
49 67 damage profiles for UN, α -U₂N₃ and UO₂ shown previously [9]. The region of interest of below 3
50
51 68 μ m is located at the common plateau portion of the damage curves of three phases, where the
52
53 69 damage dose is about 0.5~0.6 dpa for the three phases. Based on the SRIM results, the calculated
54
55
56
57
58
59
60
61
62
63
64
65

1
2
3
4 70 dose varied by only 10% across the three phases, which is within the variance expected for a single
5
6 71 phase across the depth region investigated. This depth range was selected with the purpose of
7
8
9 72 avoiding significant injected-proton-interstitial effects [46,47].
10

11 73 2.2 Microstructural Characterization

12
13
14 74 After the ion irradiation, the “lift-out” technique using focused ion beam (FIB) equipped on
15
16
17 75 an FEI Quanta 3D scanning electron microscope was conducted to prepare electron transparent
18
19 76 specimen, followed by low-energy (5 kV and 2 kV) ion sputtering to reduce FIB-induced damages
20
21
22 77 on the sample surface. Three phases, UN, α -U₂N₃, and UO₂ after irradiation at two temperatures,
23
24 78 were identified and located by performing energy-dispersive X-ray spectroscopy (EDS) mapping
25
26
27 79 using a Titan Themis 200 Scanning and Transmission Electron Microscope (S/TEM). Detailed
28
29 80 chemical mapping results with limited strain-based contrast imaging have been reported in the
30
31
32 81 previous study [9].
33

34
35 82 Dislocation loop characterization and Burgers vector analysis for the two nitride-based phases
36
37 83 were conducted with two techniques: (i) two-beam condition imaging in STEM mode using the
38
39
40 84 $\vec{g} \cdot \vec{b}$ invisibility criterion [48] involving multiple tilting conditions, and (ii) the recently
41
42 85 developed on-zone STEM imaging [36–38]. The diffraction patterns were obtained after the
43
44
45 86 sample tilting using CTEM, and then STEM was used for imaging at the selected tilting conditions.
46
47 87 The zone axes used for all the dislocation loop characterization were one of the commonly used
48
49
50 88 major low-index ones including [001], [011], and [111] because the dislocation loop morphology
51
52 89 maps are available in the literature for the FCC (similar to UN) and BCC (similar to α -U₂N₃)
53
54
55 90 crystal structures, and the \vec{g} vectors near these zone axes were selected to be low-order as well.
56
57
58
59
60
61
62
63
64
65

1
2
3
4
5
6
7
8
9
10
11
12
13
14
15
16
17
18
19
20
21
22
23
24
25
26
27
28
29
30
31
32
33
34
35
36
37
38
39
40
41
42
43
44
45
46
47
48
49
50
51
52
53
54
55
56
57
58
59
60
61
62
63
64
65

91 Dislocation loop characterization in proton irradiated UO₂ at 710°C was conducted using the
92 $\vec{g} \cdot \vec{b}$ invisibility criterion in CTEM mode. The characterization for UO₂ irradiated at 400°C was
93 not conducted because dislocation loops are too small (e.g., < 5 nm) to be identified using S/TEM
94 techniques, especially with the existence of possible FIB-induced black-dot damage.

95 3. Results

96 3.1 Dislocation Loops in UN after Irradiation at 400°C and 710°C

97 Figure 1 shows the dislocation loop structures in the UN phase after irradiation at 400°C. The
98 on-zone [001] STEM bright-field (STEM-BF) image exhibits all dislocations and dislocation loops,
99 while kinematic two-beam condition STEM-BF images utilizing $\vec{g} \cdot \vec{b}$ invisibility criterion reduce
100 or eliminate the contrast of some of the dislocation loops. Multiple \vec{g} conditions are achieved near
101 the [001] zone axis, including $\vec{g}_{\bar{2}00}$, $\vec{g}_{\bar{2}20}$, \vec{g}_{020} and $\vec{g}_{\bar{2}\bar{2}0}$. The dislocation loop morphology map
102 developed for irradiated FCC-based alloys at [001] zone axis (adapted from Ref. [38]) is shown in
103 Figure 1 as well. Because the rocksalt crystal structure of UN is similar to the FCC crystal structure,
104 similar types of dislocation loops, i.e., $a/2\langle 110 \rangle \{110\}$ perfect and $a/3\langle 111 \rangle \{111\}$ faulted loops, if
105 exist, are expected to form under irradiation.

1
2
3
4
5
6
7
8
9
10
11
12
13
14
15
16
17
18
19
20
21
22
23
24
25
26
27
28
29
30
31
32
33
34
35
36
37
38
39
40
41
42
43
44
45
46
47
48
49
50
51
52
53
54
55
56
57
58
59
60
61
62
63
64
65

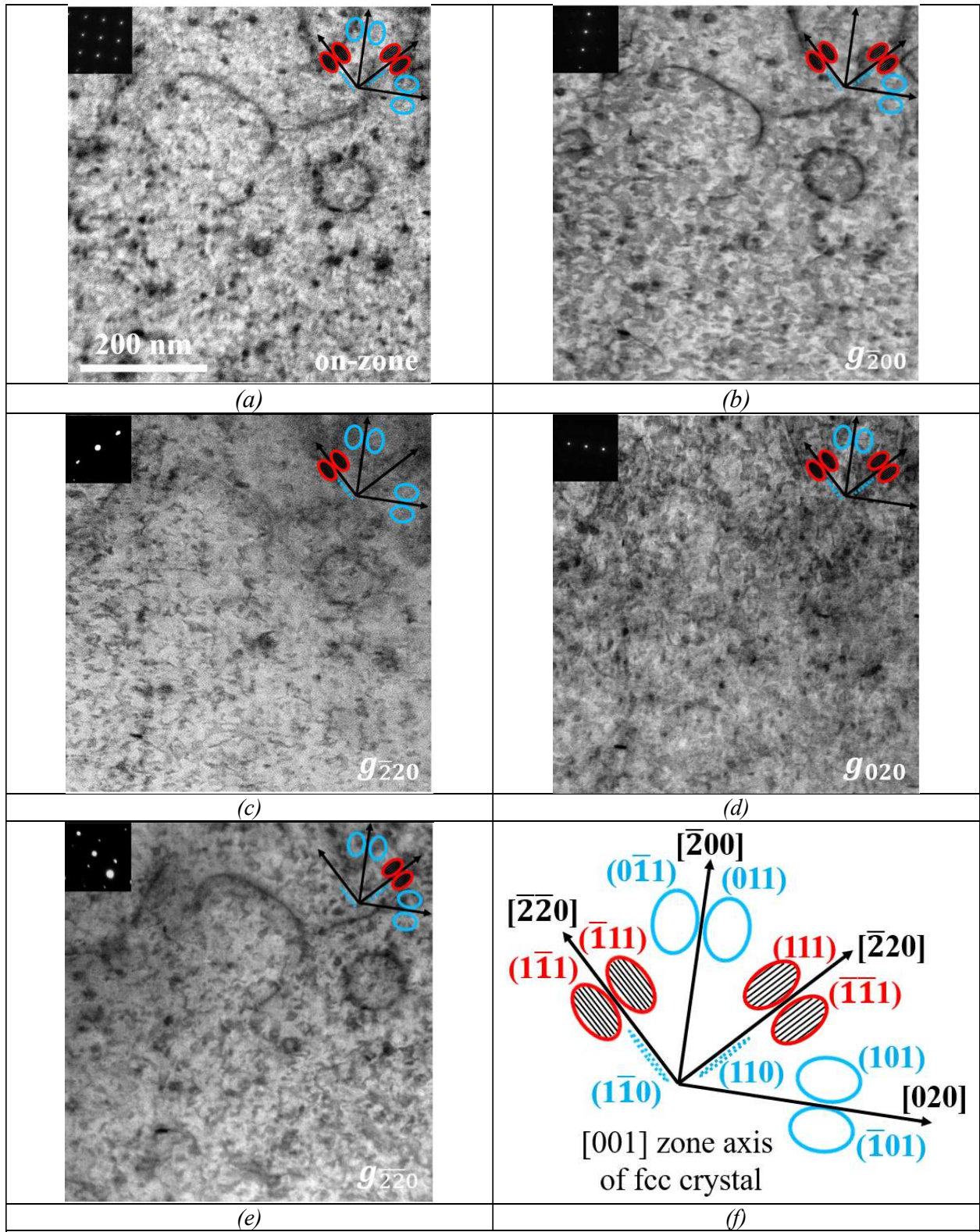


Figure 1. STEM-BF images of irradiated UN phase at 400°C with imaging conditions of (a) on-zone [001], as well as kinematic two-beam conditions with (b) \vec{g}_{200} , (c) \vec{g}_{220} , (d) \vec{g}_{020} and (e) \vec{g}_{220} , respectively. The morphology and interior contrast of the visible dislocation loops is shown at the top right corner for each imaging condition, based on the developed dislocation loop morphology map

1
2
3
4 developed for FCC based alloys at [001] zone axis (adapted from Ref. [38]). The full crystallographic
5 orientation of all the dislocation loop type is shown in (f), with its orientation rotated and correlated to
6 the STEM images in (a)~(e). Note that the $a/3\langle 111 \rangle$ faulted loops are not observed in the microstructures.
7

8 107

9
10 108 As can be seen, there is no $a/3\langle 111 \rangle$ faulted dislocation loop observed in irradiated UN at the
11
12
13 109 temperature of 400°C, because (i) the interference shadow contrast would have been exhibited if
14
15
16 110 faulted loops exist in irradiated or quenched FCC alloys [29,38,49–52] due to the inserted faulted
17
18 111 plane causing a phase change of the electron wave [48,53], and (ii) no loops appear or disappear
19
20
21 112 in the same way as the faulted dislocation loops in the STEM images of different two-beam
22
23 113 conditions that is determined by the $\vec{g} \cdot \vec{b}$ invisibility criterion. Therefore, all observed dislocation
24
25
26 114 loops are considered to be perfect-type in the irradiated UN, assuming all faulted loops would
27
28
29 115 appear non-edge-on at the [001] viewing direction.
30

31 116 The irradiation-induced dislocation loop structures at 710°C are shown in Figure 2, with the
32
33
34 117 on-zone $[\bar{1}11]$ STEM-BF image exhibits all dislocations and dislocation loops, as well as three
35
36 118 kinematic two-beam condition STEM-BF images near the $[\bar{1}11]$ zone axis with $\vec{g}_{\bar{2}0\bar{2}}$, $\vec{g}_{0\bar{2}\bar{2}}$ and
37
38
39 119 $\vec{g}_{\bar{2}\bar{2}0}$, respectively. The dislocation loop morphology map developed for irradiated FCC-based
40
41 120 alloys at $[\bar{1}11]$ zone axis (adapted from Ref. [38]) is shown in Figure 2 as well. Again, only the
42
43
44 121 perfect dislocation loops in the microstructure exist after the proton irradiation at 710°C.
45
46
47
48
49
50
51
52
53
54
55
56
57
58
59
60
61
62
63
64
65

1
2
3
4
5
6
7
8
9
10
11
12
13
14
15
16
17
18
19
20
21
22
23
24
25
26
27
28
29
30
31
32
33
34
35
36
37
38
39
40
41
42
43
44
45
46
47
48
49
50
51
52
53
54
55
56
57
58
59
60
61
62
63
64
65

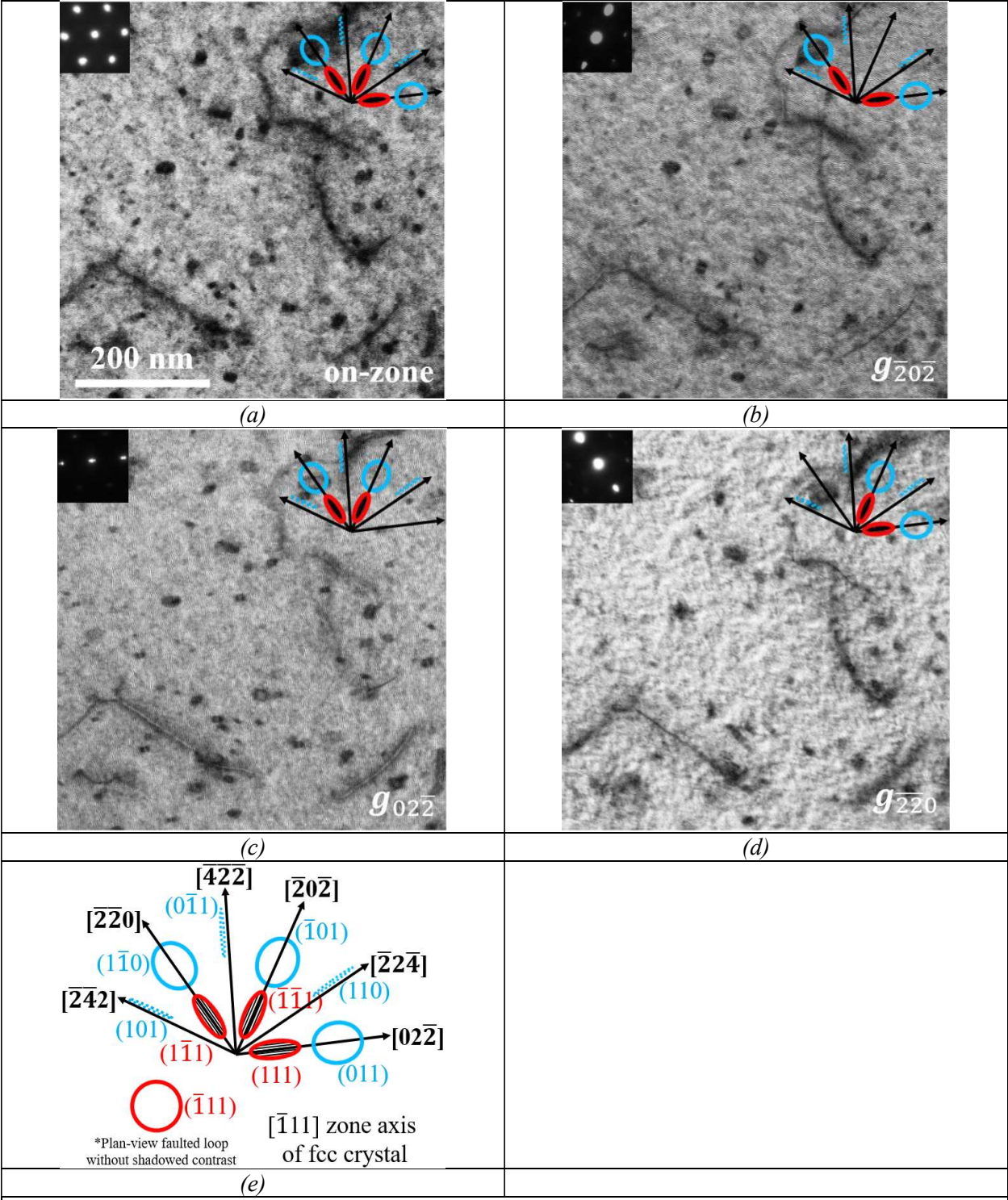


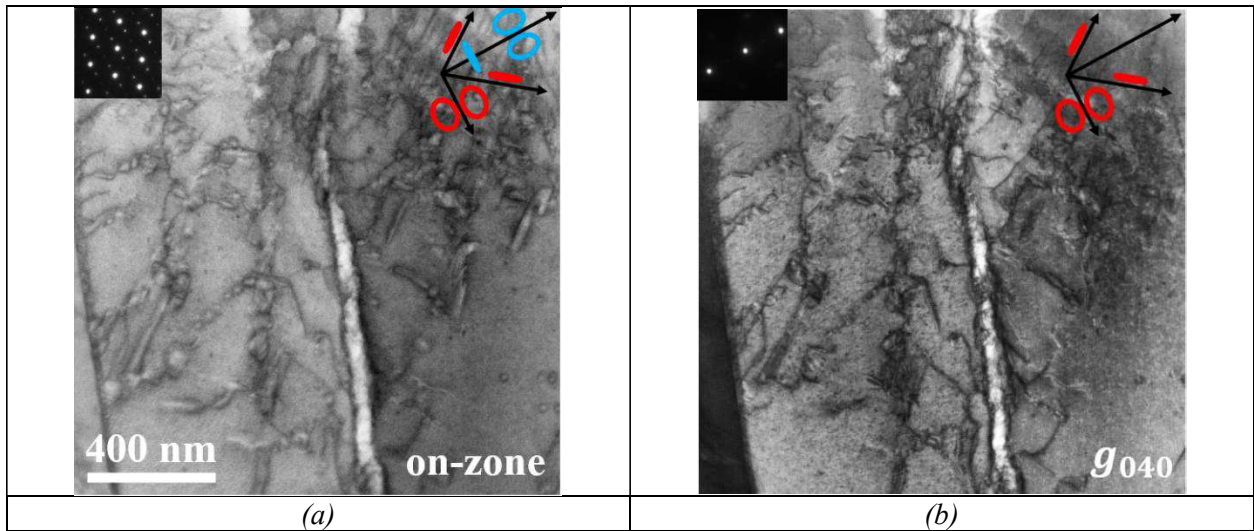
Figure 2. STEM-BF images of irradiated UN phase at 710°C with imaging conditions of (a) on-zone $[\bar{1}11]$, as well as kinematic two-beam conditions with (b) \bar{g}_{202} , (c) \bar{g}_{022} and (d) \bar{g}_{220} , respectively. The morphology and interior contrast of the visible dislocation loops is shown at the top right corner for each imaging condition, based on the developed dislocation loop morphology map developed for FCC based alloys at $[\bar{1}11]$ zone axis (adapted from Ref. [38]). The full crystallographic orientation of all the dislocation loop type is shown in (e), with its orientation rotated and correlated to the STEM images in (a)~(d). Note that the $a/3(111)$ faulted loops are not observed in the microstructures.

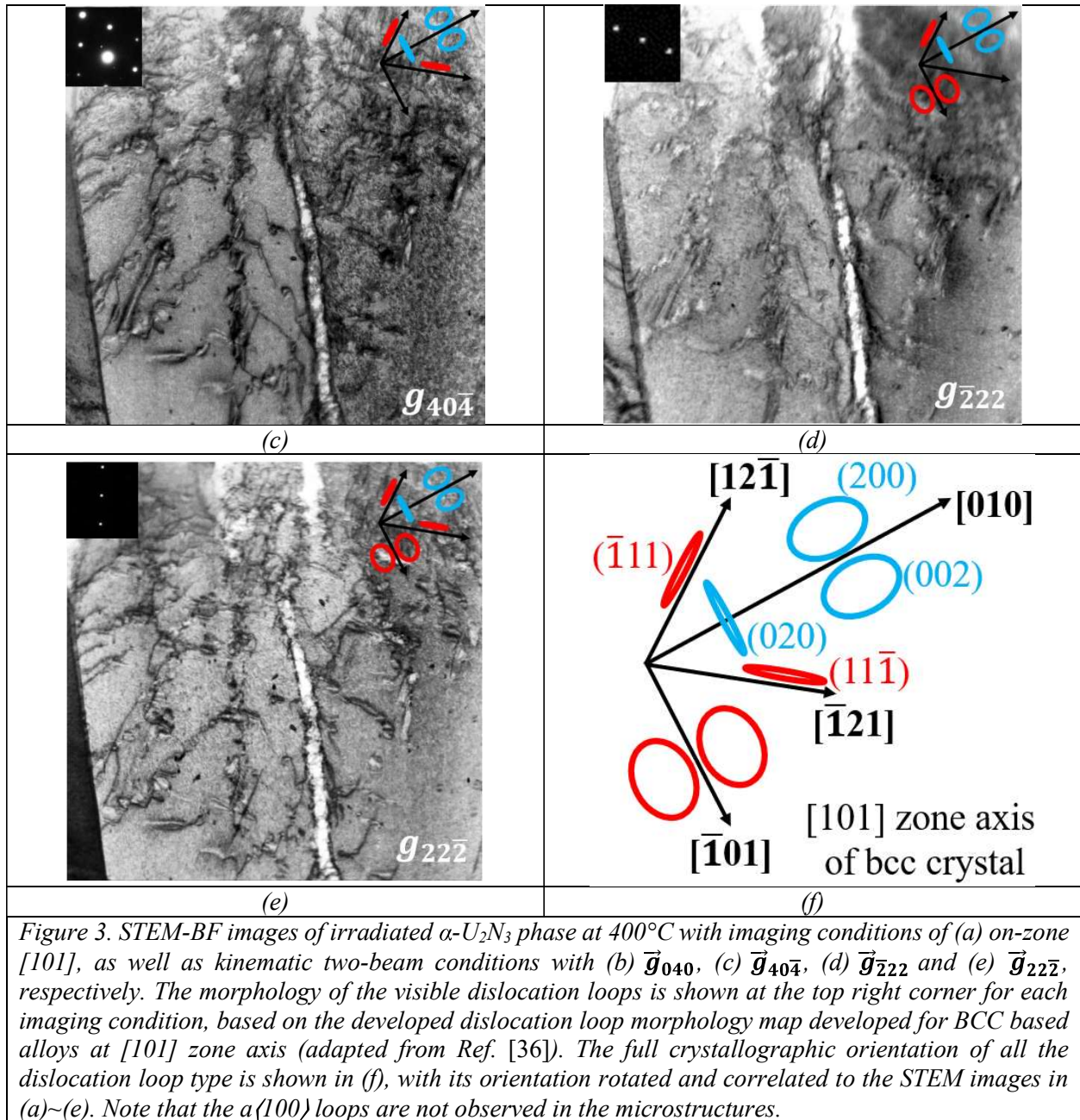
1
2
3
4
5
6
7
8
9
10
11
12
13
14
15
16
17
18
19
20
21
22
23
24
25
26
27
28
29
30
31
32
33
34
35
36
37
38
39
40
41
42
43
44
45
46
47
48
49
50
51
52
53
54
55
56
57
58
59
60
61
62
63
64
65

122

123 3.2 Dislocation Loops in α -U₂N₃ after Irradiation at 400°C and 710°C

124 The dislocation loop structures of proton irradiated α -U₂N₃ at 400°C are shown in Figure 3,
125 with the on-zone [101] STEM-BF image exhibits all dislocations and dislocation loops, as well as
126 three kinematic two-beam condition STEM-BF images near the [110] zone axis with \vec{g}_{040} , $\vec{g}_{40\bar{4}}$,
127 $\vec{g}_{\bar{2}22}$ and $\vec{g}_{22\bar{2}}$, respectively. The dislocation loop morphology map developed for irradiated BCC
128 Fe-based alloys at [101] zone axis (adapted from Ref. [36]) is shown in Figure 3(f). Because the
129 Mn₂O₃ crystal structure of the α -U₂N₃ phase is similar to the BCC crystal structure, and thus,
130 similar types of dislocation loops, i.e., a $\langle 100 \rangle \{200\}$ and $a/2\langle 111 \rangle \{111\}$, if exist, are expected
131 under irradiation.





132

133

By carefully examining the visibility of dislocation loops under all the selected two-beam conditions, as well as their morphology prediction, it is determined that only $a/2\langle 111 \rangle$ type of dislocation loops exist in the irradiated α - U_2N_3 at 400°C, while $a\langle 100 \rangle$ loops are not observed.

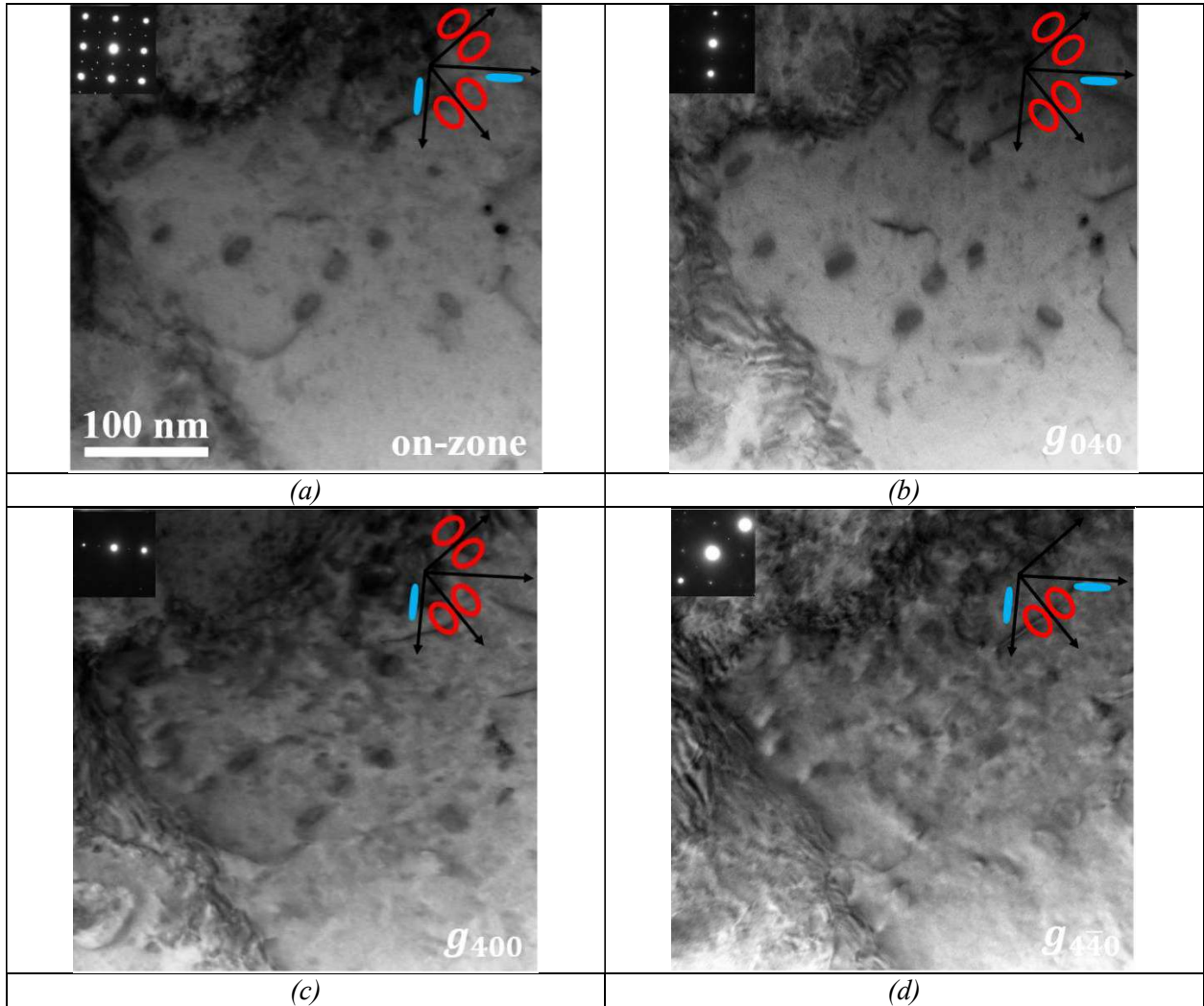
135

136

In addition, all the dislocations are also identified with the type of $a/2\langle 111 \rangle$.

1
2
3
4
5
6
7
8
9
10
11
12
13
14
15
16
17
18
19
20
21
22
23
24
25
26
27
28
29
30
31
32
33
34
35
36
37
38
39
40
41
42
43
44
45
46
47
48
49
50
51
52
53
54
55
56
57
58
59
60
61
62
63
64
65

137 At a higher temperature of 710°C, the proton irradiation-induced dislocation loop structures
138 are shown in Figure 4 in corresponding STEM images. In this case again, only the $a/2\langle 111 \rangle$ type
139 dislocation loops are identified from the elliptical shape and the direction of the major axis
140 observed, and by the comparison with the dislocation loop morphology map in Figure 4(f).



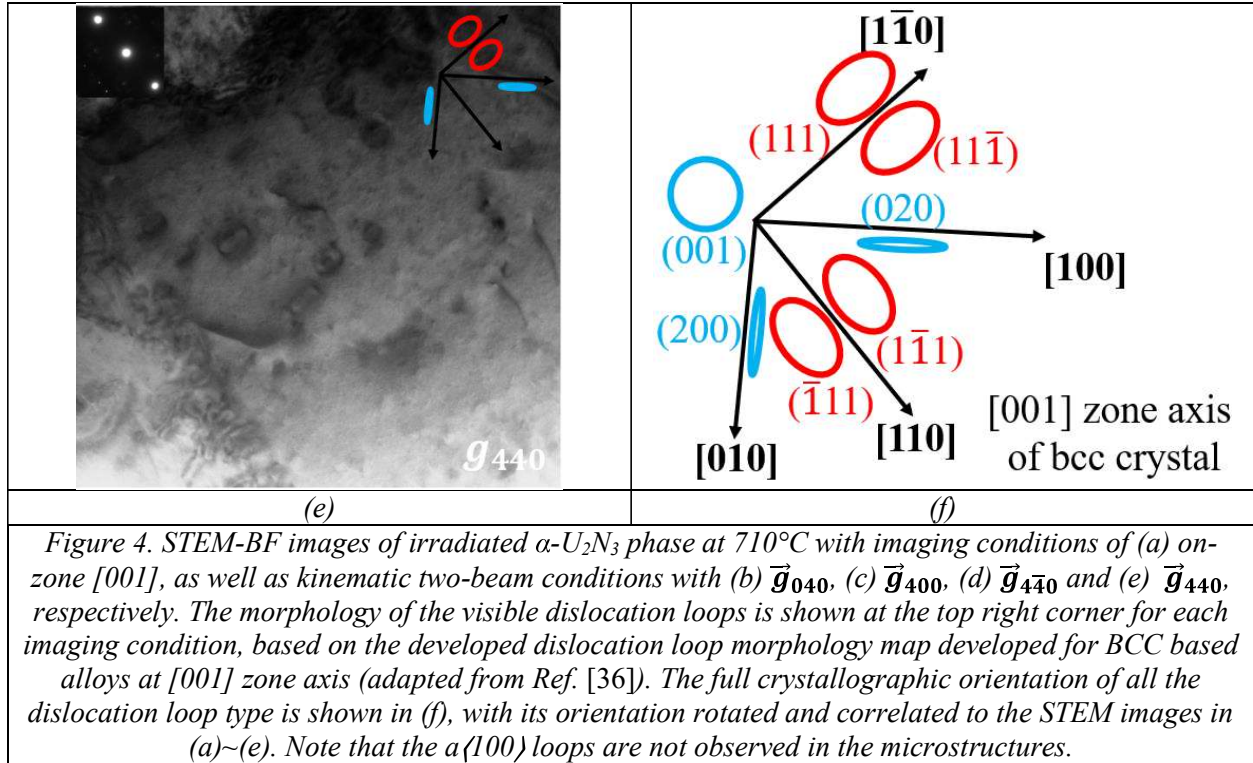


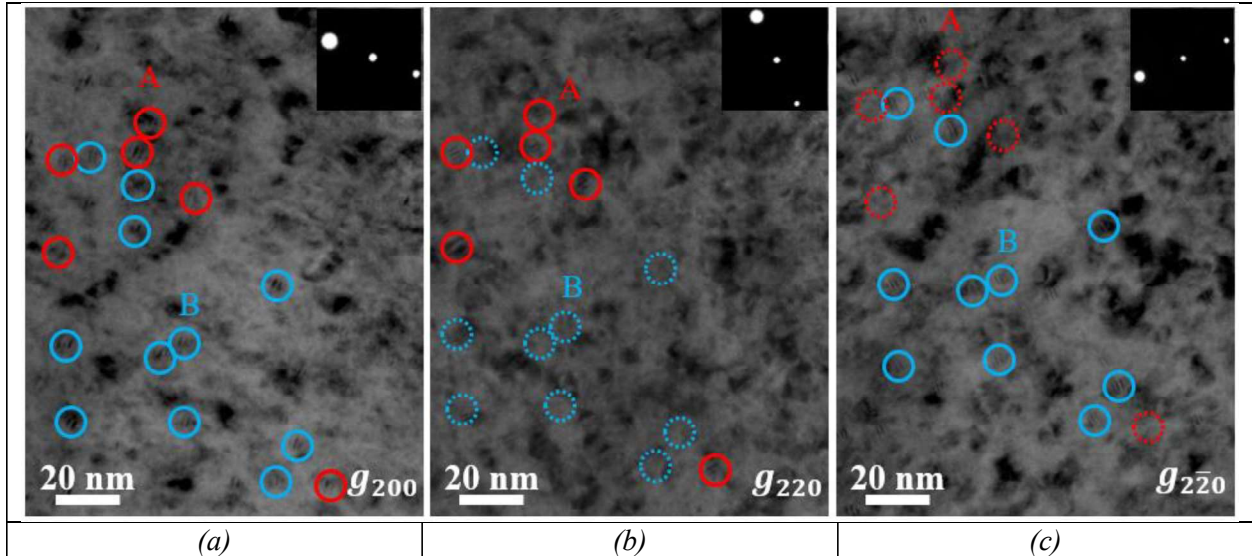
Figure 4. STEM-BF images of irradiated α - U_2N_3 phase at 710°C with imaging conditions of (a) on-zone $[001]$, as well as kinematic two-beam conditions with (b) \vec{g}_{040} , (c) \vec{g}_{400} , (d) $\vec{g}_{4\bar{4}0}$ and (e) \vec{g}_{440} , respectively. The morphology of the visible dislocation loops is shown at the top right corner for each imaging condition, based on the developed dislocation loop morphology map developed for BCC based alloys at $[001]$ zone axis (adapted from Ref. [36]). The full crystallographic orientation of all the dislocation loop type is shown in (f), with its orientation rotated and correlated to the STEM images in (a)–(e). Note that the $a\{100\}$ loops are not observed in the microstructures.

3.3 Dislocation Loops in UO_2 after Irradiation at 710°C

The dislocation loop structures of proton irradiated UO_2 at 710°C are shown in Figure 5, with the Burgers vector analysis conducted by using the $\vec{g} \cdot \vec{b}$ invisibility criterion in the CTEM mode. This technique was chosen for loop type analysis in irradiated UO_2 over the previously mentioned morphology-based technique, because as can be seen in Figure 5, the dislocation loop size is quite small (< 5 nm), making the morphology ambiguous to identify.

Figure 5 shows CTEM-BF images of UO_2 phase obtained using various g conditions near $[001]$ zone axis, including \vec{g}_{200} , \vec{g}_{220} and $\vec{g}_{2\bar{2}0}$. Table 1 shows invisibility criteria for dislocation loops with four variants of $a/3\langle 111 \rangle$ faulted type and six variants of $a/2\langle 110 \rangle$ perfect type Burgers vector directions under the three selected \vec{g} two-beam conditions. In Figure 5, two different families of dislocation loops were identified by letters A and B and colors red and yellow, respectively. Family

1
2
3
4 153 A dislocation loops were visible at \vec{g}_{200} and \vec{g}_{220} , while became invisible at $\vec{g}_{2\bar{2}0}$ as shown in
5
6
7 154 Figure 5(a), 5(b) and 5(c), respectively. Family B dislocation loops were visible at \vec{g}_{200} and $\vec{g}_{2\bar{2}0}$
8
9
10 155 while disappears at \vec{g}_{220} as shown in Figure 5(a), 5(b) and 5(c), respectively. Table 1 also lists
11
12 156 possible Burgers vector directions for loop family A and B based on their appearances and
13
14 157 disappearances at given \vec{g} conditions. Burgers vector direction of loop family A was either [111]
15
16
17 158 or $[\bar{1}\bar{1}1]$ or [110], while Burgers vector direction of loop family B was either $[1\bar{1}\bar{1}]$ or $[1\bar{1}1]$ or
18
19 159 $[\bar{1}10]$, as shown in Table 1. It should be noted that current \vec{g} conditions identify both loop families
20
21
22 160 A and B as either $a/3\langle 111 \rangle$ type faulted dislocation loops or $a/2\langle 110 \rangle$ type perfect dislocation loops.



23
24
25
26
27
28
29
30
31
32
33
34
35
36
37
38
39
40
41
42
43 *Figure 5. CTEM-BF images of irradiated UO_2 phase at $710^\circ C$ with imaging conditions of kinematic two-beam conditions with (a) \vec{g}_{200} , (b) \vec{g}_{220} , and (c) $\vec{g}_{2\bar{2}0}$ near the $[001]$ zone axis. Note that the dislocation loop size in the irradiated UO_2 phase is so small that the morphology-based technique mentioned before may not readily apply due to the ambiguous observed dislocation loop morphology.*

44
45
46
47
48 161
49
50
51 162 **Table 1.** Burgers vector analysis using $\vec{g} \cdot \vec{b} = 0$ invisibility criterion for the proton irradiated UO_2 phase
52
53 163 at $710^\circ C$.

\vec{b}	\vec{g} (zone axis = $[001]$)			Identified loops
	$[200]$	$[220]$	$[2\bar{2}0]$	
$a/3[111]$	V	V	I	A ●
$a/3[\bar{1}\bar{1}1]$	V	V	I	A ●
$a/3[1\bar{1}\bar{1}]$	V	I	V	B ●
$a/3[\bar{1}\bar{1}1]$	V	I	V	B ●

a/2[011]	I	V	V	–
a/2[101]	V	V	V	–
a/2[110]	V	V	I	A
a/2[0 $\bar{1}$ 1]	I	V	V	–
a/2[10 $\bar{1}$]	V	V	V	–
a/2[$\bar{1}$ 10]	V	I	V	B 

164

165

166

167

168

169

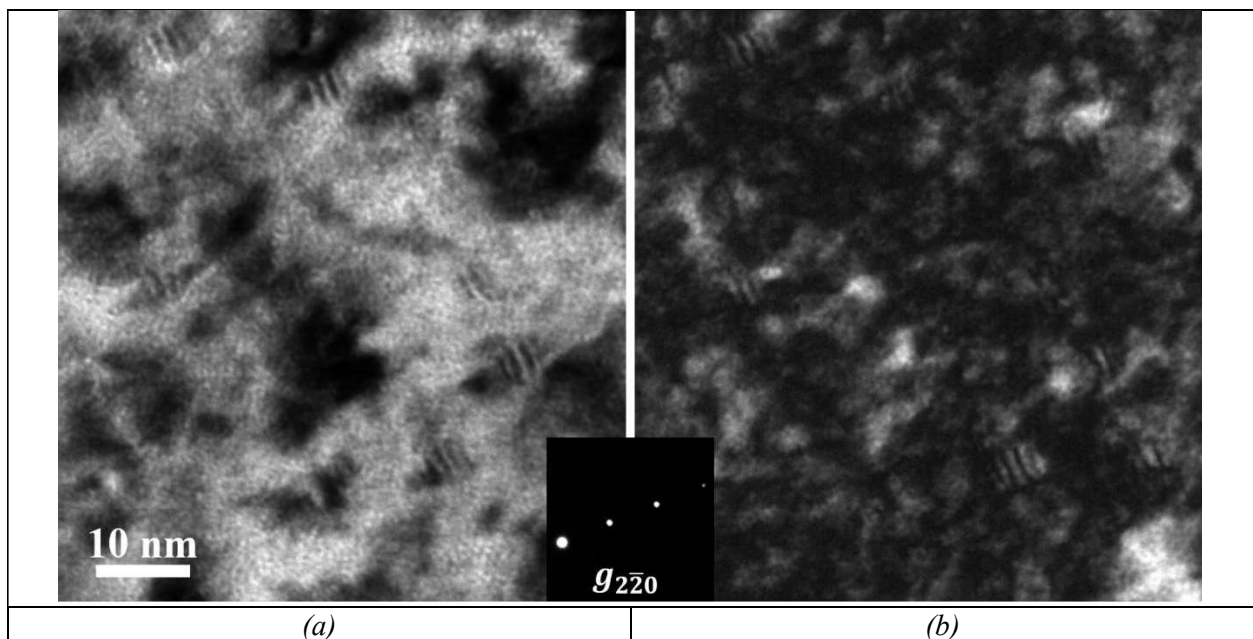
170

171

172

173

To further confirm the dislocation loop type, high magnification CTEM-BF and weak beam dark field (WBDF) images of dislocation loops in the irradiated UO₂ phase at $g = [2\bar{2}0]$ near [001] zone axis are shown in Figure 6(a) and 6(b), respectively. It is seen that dislocation loops have elliptical shape with stacking fault fringes inside of it. Since only faulted $a/3\langle 111 \rangle$ type dislocation loops can contribute the inserted extra plane that causes faulted stacking sequence, it can be concluded that loop family A and loop family B are of different variants, but both are $a/3\langle 111 \rangle$ type faulted dislocation loops. This observation is in good agreement with the proton irradiation ThO₂ in the previous study [34], where only $a/3\langle 111 \rangle$ type of faulted dislocation loops were found.



1
2
3
4
5
6
7
8
9
10
11
12
13
14
15
16
17
18
19
20
21
22
23
24
25
26
27
28
29
30
31
32
33
34
35
36
37
38
39
40
41
42
43
44
45
46
47
48
49
50
51
52
53
54
55
56
57
58
59
60
61
62
63
64
65

174

Figure 6. CTEM- (a) BF and corresponding (b) weak beam dark field (WBDF) images of UO₂ phase irradiated at 710°C obtained using $\vec{g}_{2\bar{2}0}$ near the [001] zone axis.

175 4. Discussion

176 To examine the structure and energetics of the two types of dislocation loops in UN, we applied
177 molecular statics (MS) calculation using the LAMMPS package (<https://lammps.sandia.gov>) [54].
178 The interatomic potential considering the angular dependence was developed by Tseplyaev and
179 Starikov [55], based on force-matching to DFT database. This potential was demonstrated to have
180 a low fitting error and well-reproduced thermodynamic properties for the B1-phase of UN [55].
181 Therefore, this potential is utilized. Note that it does not explicitly consider charge property, which
182 may be justified by the fact that the bonding between U and N atoms is metallic-like [56].

183 In the crystal structure of B1-phase, there are predominantly two types of dislocation loops
184 formed under irradiation, i.e. $a/3\langle 111 \rangle$ faulted loops and $a/2\langle 110 \rangle$ perfect loops. Notably, the
185 faulted loops have been reported in irradiated titanium carbide (TiC) [57,58], zirconium carbide
186 (ZrC) [59] and high-entropy carbide [60]. Here, we consider pure-edge type $a/3\langle 111 \rangle$ and $a/2\langle 110 \rangle$
187 loops on $\{111\}$ and $\{110\}$ habit planes, respectively. To ease the construction of loops, perfect
188 simulation cells with z-axis oriented in [111] ($15.2 \text{ nm} \times 15.5 \text{ nm} \times 10.1 \text{ nm}$, 164,736 atoms) and
189 [011] directions ($15.6 \text{ nm} \times 15.2 \text{ nm} \times 10.3 \text{ nm}$, 168,960 atoms) are created and relaxed to ground
190 state, respectively.

191 To study the energetics of perfect and faulted dislocation loops in UN, we need to first identify
192 the atomic structure for the loops. For $a/3\langle 111 \rangle$ loop, due to the electrostatic interaction, a single
193 layer of $\{111\}$ loop would be energetically prohibited. With double layer $\{111\}$ loops, the
194 stoichiometry can significantly reduce the energy penalty. In this case, there are a few possible

1
2
3
4
5
6
7
8
9
10
11
12
13
14
15
16
17
18
19
20
21
22
23
24
25
26
27
28
29
30
31
32
33
34
35
36
37
38
39
40
41
42
43
44
45
46
47
48
49
50
51
52
53
54
55
56
57
58
59
60
61
62
63
64
65

195 stacking sequences for the $a/3\langle 111 \rangle$ loops, which are demonstrated in Figure 7. Figure 7(a) shows
196 the perfect stacking. By comparison, Figure 7(b-d) indicate two inserted atomic layers (U and N
197 layer) differently: “S” denotes normal stacking in the sublattice leading to a standard stack fault
198 and “OS” denotes overlapping stacking, which would be prohibited in an FCC structure, but can
199 be stabilized with interweaving atomic layers with an opposite charge. Using the same notation
200 for the insert layers, Figure 8 compares the formation energy of a loop with 3 nm in diameter (the
201 only difference lies in the stacking). Figure 7(d) corresponds to the lowest energy configuration.
202 With this stacking, the stacking fault energy (γ) is calculated to be 1.54 J/m^2 . Also, such stacking
203 is used for the energetic calculations for faulted loops at different sizes. For $a/2\langle 110 \rangle$ loop, the
204 double-layer $\{110\}$ stacking is shown in Figure 9, with each layer containing an equal number of
205 interstitials of both atom types. After identifying the stacking, loops at different radii are created
206 in the shape of disk in the simulation box. Then the system is relaxed during an energy
207 minimization so that the system pressure tensor is reduced to zero; this is followed by multiple
208 rounds of static minimization with conjugate gradient method.

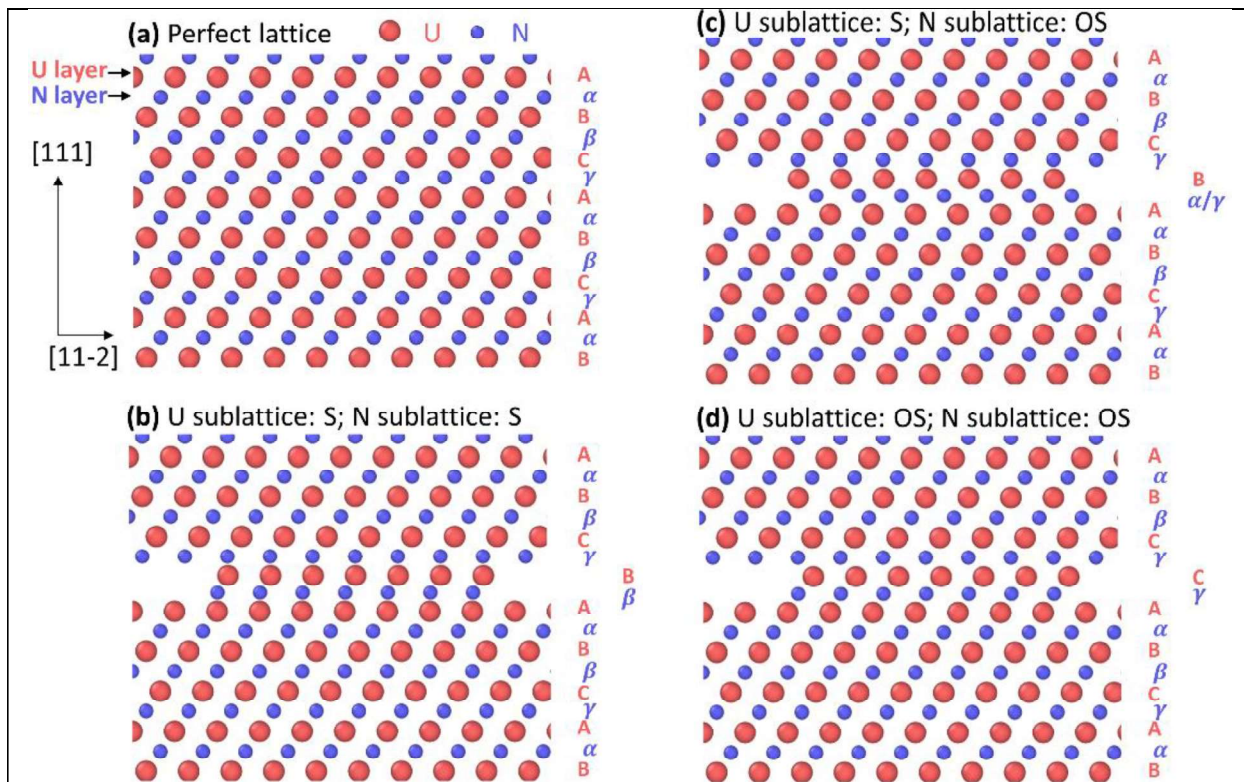


Figure 7. (a) Perfect lattice stacking; (c-d) different stacking for the inserted two layers (U and N layers, shape in disk). S: normal stacking in the sublattice; OS: overlapping stacking in the sublattice.

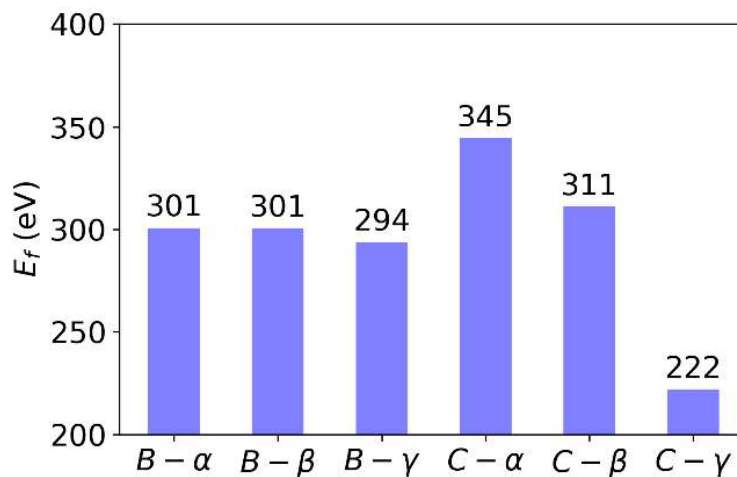
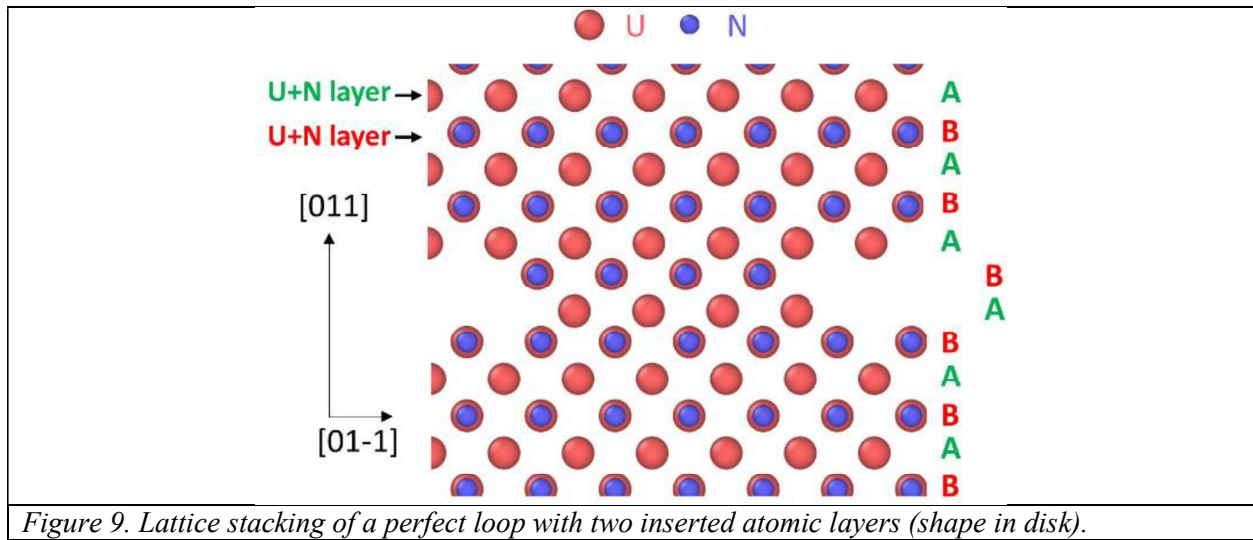
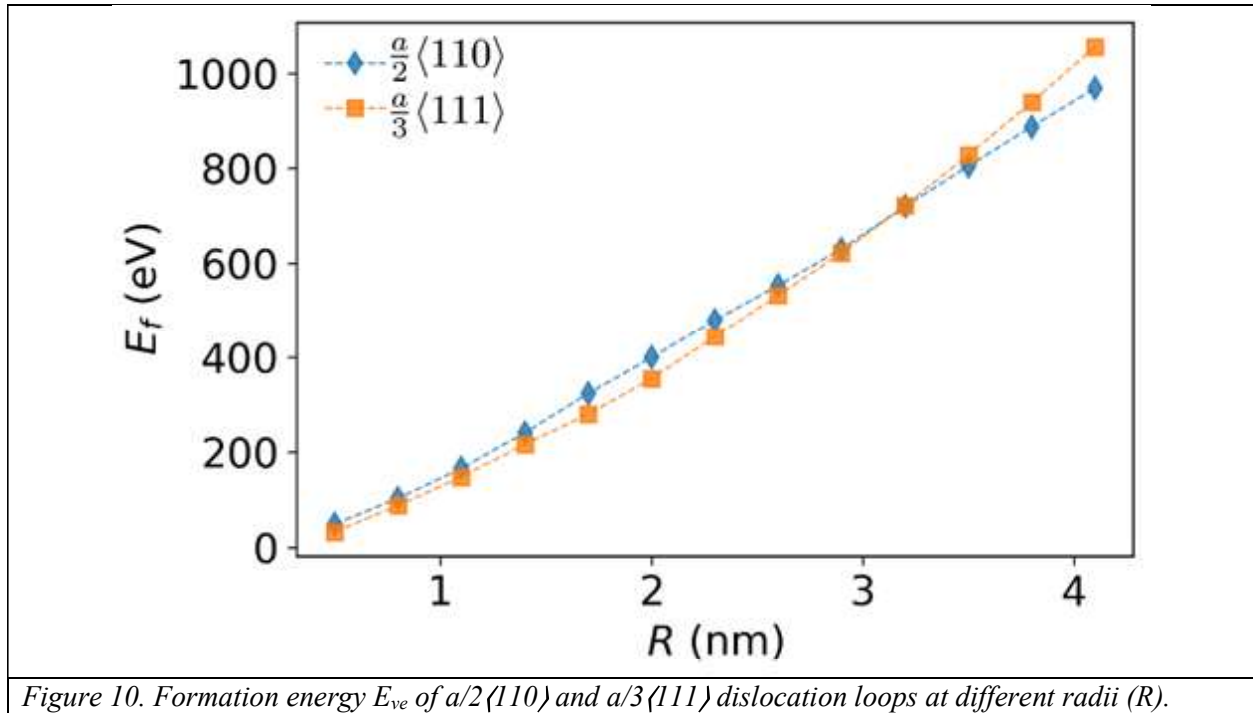


Figure 8. Formation energy of 3.0 nm diameter faulted loops for different stacking. The labels denote the stacking of the two insert atomic layers (see Figure 7b-d). Lowest energy (C- γ) corresponds to Figure 7(d).



The loop formation energies are compared as a function of loop size as shown in Figure 10. It is expected that the faulted loop becomes energetically less favorable as loop size increases, because of the energy penalty from stacking fault [61]. As the loop size is below ~6 nm in diameter, $a/3\langle 111 \rangle$ extrinsic loop is slightly energetically favorable, while as the size becomes larger, there is an energetic preference to transform to a perfect loop. This can be achieved by nucleating Shockley partial dislocations [62] to initiate the unfauling process. Note that due to the energy barrier of dislocation nucleation and migration [62], one may observe large faulted loops, especially at low temperatures without deformation. Although the average dislocation loop size is 6.2 ± 1.7 nm at 400°C [9], which is close to the critical size of ~6 nm calculated by MS simulation, $a/3\langle 111 \rangle$ faulted loops were not observed in this work. The observation indicates the unfauling process of dislocation loops in irradiated UN might happen at even smaller size. A similar unfauling process has been observed in neutron [63] and proton [59] irradiated ZrC, where ZrC shares the same crystal structure as UN. Faulted dislocation loops formed with the average size of 4.3 ± 0.5 nm and 5.8 ± 0.6 nm in proton irradiated ZrC up to 0.7 dpa and 1.5 dpa, respectively, at 800°C [59], while only unfaulted perfect dislocation loops with the average size of 9.85 nm were

228 observed in proton irradiated zorch up to 2 dpa at 1125°C [64]. Therefore, to reveal the unfaulting
 229 process in UN, proton irradiation experiment at lower temperature, i.e. <400°C, or lower dose,
 230 needs to be pursued in future studies.



231
 232 In this study, only $a/2\langle 111\rangle$ type of dislocation loops formed after proton irradiation at two
 233 temperatures in α - U_2N_3 that has a Mn_2O_3 -type BCC crystal structure. It has been extensively
 234 reported in BCC-based ferritic alloys that perfect $a/2\langle 111\rangle$ and $a\langle 100\rangle$ loops can form under
 235 irradiation [65–73]. It would have been interesting to compare the formation energy of these two
 236 types of dislocation loops in α - U_2N_3 using MS calculation, but the interatomic potential of α - U_2N_3
 237 has not been developed. Similar $a/2\langle 111\rangle$ perfect dislocation loop formation was observed in In_2O_3
 238 [74] that has the same Mn_2O_3 -type BCC crystal structure, where these loops formed from
 239 misfitting inclusions at smaller misfit values than straight dislocations during In_2O_3 nanorod
 240 growth rather than under irradiation. To fully understand the defect evolution under irradiation in

1
2
3
4 241 α -U₂N₃, the loop formation mechanism needs to be further explored via well-designed experiments
5
6 242 and modeling.
7
8

9
10 243 The dislocation loop type in proton irradiated UO₂ is in good agreement with that in proton
11
12 244 irradiated ThO₂, where only $a/3\langle 111 \rangle$ faulted dislocation loops were found [34]. The average loop
13
14 245 size is quite small of 3.3 nm [9] and 4.5 nm [34] in proton irradiated UO₂ and ThO₂, respectively.
15
16
17 246 On the contrary, only $a/2\langle 110 \rangle$ perfect loops of larger size were observed in heavy ion irradiated
18
19 247 UO₂ [17–19] and ThO₂ [35]. Similar to UN, MD calculations of loop formation energy in UO₂
20
21 248 [21,22] and ThO₂ [35] indicate that, $a/3\langle 111 \rangle$ faulted dislocation loops are energetically favorable
22
23
24 249 when their size is less than a few nanometers, above which the unfauling process may occur.
25
26

27
28 250 Irradiation induced defects may affect mechanical and thermal properties of ceramic nuclear
29
30 251 fuels and their non-radioactive surrogate, cerium dioxide (CeO₂) [75–81]. The thermal transport
31
32 252 behavior in CeO₂ is significantly affected by the type of dislocation loops, where perfect loops
33
34 253 only slightly reduce the thermal conductivity while faulted loops lead to an unusually large
35
36
37 254 reduction of thermal conductivity [77]. This was ascribed to extensive phonon scattering because
38
39
40 255 of a stronger strain field surrounding faulted loops. The effects of loop type and size on thermal
41
42 256 conductivity may also exist in UN, and more efforts on this topic are needed in the future.
43
44

45 257 **5. Conclusion**

46
47
48 258 The dislocation loop type analysis in proton irradiated UN and α -U₂N₃ phases at 400°C and
49
50
51 259 710°C, as well as irradiated UO₂ at 710°C are systematically investigated. It is revealed that a
52
53 260 single dislocation loop type of $a/2\langle 110 \rangle$, $a/2\langle 111 \rangle$ and $a/3\langle 111 \rangle$ exists in UN, α -U₂N₃ and UO₂
54
55
56 261 phases, respectively. For the UN phase, MS simulation reveals that the formation energy of
57
58 262 $a/3\langle 111 \rangle$ faulted loops is lower than $a/2\langle 110 \rangle$ perfect loops when the dislocation loop size is smaller
59
60
61

1
2
3
4 263 than 6 nm, which is well below the resolution limit of the selected STEM imaging condition; it
5
6
7 264 explains why only perfect type of dislocation loops are observed in UN at two test temperatures.
8
9 265 This result is the first to report the single dislocation loop type formed in the proton irradiated
10
11 266 uranium nitrides and uranium dioxide phases, though future work concerning different radiation
12
13
14 267 conditions may be conducted to further investigate other potential dislocation loop type formation
15
16 268 in the systems.
17
18
19
20 269

21 22 270 **Acknowledgements**

23
24
25 271 The microstructural characterization was supported by the U.S. Department of Energy, Office
26
27 272 of Nuclear Energy under DOE Idaho Operations Office Contract DEAC07-05ID14517 as part of
28
29
30 273 Nuclear Science User Facilities. The MD/MS simulation was supported by the Center for Thermal
31
32
33 274 Energy Transport under Irradiation (TETI), an Energy Frontier Research Center funded by the U.S.
34
35 275 Department of Energy (DOE), Office of Science, Basic Energy Sciences (BES). The synthesis and
36
37
38 276 ion irradiation of UN-UO₂ samples were supported by the U.S. Department of Energy, Office of
39
40 277 Nuclear Energy under a Nuclear Energy University Program (award number: DE-NE00120690).
41
42

43 278 44 45 46 279 **References**

- 47
48
49 280 [1] M. Streit, F. Ingold, Nitrides as a nuclear fuel option, *J. Eur. Ceram. Soc.* 25 (2005) 2687–
50 281 2692. <https://doi.org/10.1016/j.jeurceramsoc.2005.03.181>.
51
52 282 [2] V.M. Troyanov, A.F. Grachev, L.M. Zabud'ko, M. V. Skupov, Prospects for Using
53 283 Nitride Fuel in Fast Reactors with a Closed Nuclear Fuel Cycle, *At. Energy.* 117 (2014)
54 284 85–91. <https://doi.org/10.1007/s10512-014-9893-1>.
55
56
57 285 [3] C. Ekberg, D. Ribeiro Costa, M. Hedberg, M. Jolkkonen, Nitride fuel for Gen IV nuclear
58 286 power systems, *J. Radioanal. Nucl. Chem.* 318 (2018) 1713–1725.
59 287 <https://doi.org/10.1007/s10967-018-6316-0>.
60
61

1
2
3
4 288 [4] J.P. Gorton, B.S. Collins, A.T. Nelson, N.R. Brown, Reactor performance and safety
5 289 characteristics of ThN-UN fuel concepts in a PWR, *Nucl. Eng. Des.* 355 (2019) 110317.
6 290 <https://doi.org/10.1016/j.nucengdes.2019.110317>.
7
8
9 291 [5] D.J. Allen, S.R. Blair, M.G. Millett, M.E. Nelson, Evaluation of Non-Oxide Fuel for
10 292 Fission-Based Nuclear Reactors on Spacecraft, *Nucl. Technol.* 205 (2019) 755–765.
11 293 <https://doi.org/10.1080/00295450.2018.1524228>.
12
13 294 [6] J.T. White, A.W. Travis, J.T. Dunwoody, A.T. Nelson, Fabrication and thermophysical
14 295 property characterization of UN/U₃Si₂ composite fuel forms, *J. Nucl. Mater.* 495 (2017)
15 296 463–474. <https://doi.org/10.1016/j.jnucmat.2017.08.041>.
16
17 297 [7] K.A. Terrani, B.C. Jolly, J.M. Harp, Uranium nitride tristructural-isotropic fuel particle, *J.*
18 298 *Nucl. Mater.* 531 (2020) 152034. <https://doi.org/10.1016/j.jnucmat.2020.152034>.
19
20 299 [8] L.G. Gonzalez Fonseca, M. Hedberg, L. Huan, P. Olsson, T. Retegan Vollmer,
21 300 Application of SPS in the fabrication of UN and (U,Th)N pellets from microspheres, *J.*
22 301 *Nucl. Mater.* 536 (2020) 152181. <https://doi.org/10.1016/j.jnucmat.2020.152181>.
23
24 302 [9] L. He, M. Khafizov, C. Jiang, B. Tyburska-Püschel, B.J. Jaques, P. Xiu, P. Xu, M.K.
25 303 Meyer, K. Sridharan, D.P. Butt, J. Gan, Phase and defect evolution in uranium-nitrogen-
26 304 oxygen system under irradiation, *Acta Mater.* 208 (2021) 116778.
27 305 <https://doi.org/10.1016/j.actamat.2021.116778>.
28
29
30 306 [10] A. Gonzales, J.K. Watkins, A.R. Wagner, B.J. Jaques, E.S. Sooby, Challenges and
31 307 opportunities to alloyed and composite fuel architectures to mitigate high uranium density
32 308 fuel oxidation: uranium silicide, *J. Nucl. Mater.* (2021) 153026.
33 309 <https://doi.org/10.1016/j.jnucmat.2021.153026>.
34
35
36 310 [11] P.E. Evans, T.J. Davies, Uranium nitrides, *J. Nucl. Mater.* (1963).
37 311 [https://doi.org/10.1016/0022-3115\(63\)90115-6](https://doi.org/10.1016/0022-3115(63)90115-6).
38
39 312 [12] B.T.M. Willis, Structures of UO₂, UO_{2+x} and U₄O₉ by neutron diffraction, *J. Phys.* 25
40 313 (1964). <https://doi.org/10.1051/jphys:01964002505043100>.
41
42 314 [13] Y. Yang, C.A. Dickerson, T.R. Allen, Radiation stability of ZrN under 2.6MeV proton
43 315 irradiation, *J. Nucl. Mater.* 392 (2009) 200–205.
44 316 <https://doi.org/10.1016/j.jnucmat.2009.03.040>.
45
46
47 317 [14] L. Jiao, K.Y. Yu, D. Chen, C. Jacob, L. Shao, X. Zhang, H. Wang, Radiation tolerant
48 318 nanocrystalline ZrN films under high dose heavy-ion irradiations, *J. Appl. Phys.* 117
49 319 (2015) 145901. <https://doi.org/10.1063/1.4917381>.
50
51 320 [15] W. Bao, S. Robertson, J.-X. Liu, G.-J. Zhang, F. Xu, H. Wu, Structural integrity and
52 321 characteristics at lattice and nanometre levels of ZrN polycrystalline irradiated by 4 MeV
53 322 Au ions, *J. Eur. Ceram. Soc.* 38 (2018) 4373–4383.
54 323 <https://doi.org/10.1016/j.jeurceramsoc.2018.05.013>.
55
56
57 324 [16] A.D. Whapham, B.E. Sheldon, Radiation damage in uranium dioxide, *Philos. Mag.* 12
58 325 (1965) 1179–1192. <https://doi.org/10.1080/14786436508228669>.
59
60 326 [17] L.F. He, M. Gupta, C.A. Yablinsky, J. Gan, M.A. Kirk, X.M. Bai, J. Pakarinen, T.R.

1
2
3
4 327 Allen, In situ TEM observation of dislocation evolution in Kr-irradiated UO₂ single
5 328 crystal, *J. Nucl. Mater.* (2013). <https://doi.org/10.1016/j.jnucmat.2013.06.050>.

7 329 [18] C. Onofri, C. Sabathier, C. Baumier, C. Bachelet, H. Palancher, M. Legros, Evolution of
8 extended defects in polycrystalline Au-irradiated UO₂ using in situ TEM: Temperature
9 330 and fluence effects, *J. Nucl. Mater.* (2016). <https://doi.org/10.1016/j.jnucmat.2016.10.011>.
10 331

12 332 [19] C. Onofri, M. Legros, J. L  chelle, H. Palancher, C. Baumier, C. Bachelet, C. Sabathier,
13 333 Full characterization of dislocations in ion-irradiated polycrystalline UO₂, *J. Nucl. Mater.*
14 334 (2017). <https://doi.org/10.1016/j.jnucmat.2017.07.043>.

16 335 [20] J. Soullard, Mise en evidence de boucles de dislocation imparfaites dans des echantillons
17 336 de bioxyde d'uranium irradi  s, *J. Nucl. Mater.* 78 (1978) 125–130.
18 337 [https://doi.org/10.1016/0022-3115\(78\)90511-1](https://doi.org/10.1016/0022-3115(78)90511-1).

20 338 [21] A. Le Prioux, P. Fossati, S. Maillard, T. Jourdan, P. Maugis, Empirical potential
21 339 simulations of interstitial dislocation loops in uranium dioxide, *J. Nucl. Mater.* 479 (2016)
22 340 576–584. <https://doi.org/10.1016/j.jnucmat.2016.07.046>.

25 341 [22] A. Chartier, C. Onofri, L. Van Brutzel, C. Sabathier, O. Dorosh, J. Jagielski, Early stages
26 342 of irradiation induced dislocations in uranium, *Appl. Phys. Lett.* 109 (2016) 181902.
27 343 <https://doi.org/10.1063/1.4967191>.

29 344 [23] X.-Y. Liu, D.A. Andersson, Small uranium and oxygen interstitial clusters in UO₂: An
30 345 empirical potential study, *J. Nucl. Mater.* 547 (2021) 152783.
31 346 <https://doi.org/10.1016/j.jnucmat.2021.152783>.

33 347 [24] C. Lu, T. Yang, K. Jin, N. Gao, P. Xiu, Y. Zhang, F. Gao, H. Bei, W.J. Weber, K. Sun, Y.
34 348 Dong, L. Wang, Radiation-induced segregation on defect clusters in single-phase
35 349 concentrated solid-solution alloys, *Acta Mater.* 127 (2017) 98–107.
36 350 <https://doi.org/10.1016/j.actamat.2017.01.019>.

39 351 [25] L. Zhang, C. Lu, G. Michal, G. Deng, K. Tieu, The formation and destruction of stacking
40 352 fault tetrahedron in fcc metals: A molecular dynamics study, *Scr. Mater.* 136 (2017) 78–
41 353 82. <https://doi.org/10.1016/j.scriptamat.2017.04.019>.

43 354 [26] C. Lu, T. Yang, L. Niu, Q. Peng, K. Jin, M.L. Crespillo, G. Velisa, H. Xue, F. Zhang, P.
44 355 Xiu, Y. Zhang, F. Gao, H. Bei, W.J. Weber, L. Wang, Interstitial migration behavior and
45 356 defect evolution in ion irradiated pure nickel and Ni-xFe binary alloys, *J. Nucl. Mater.* 509
46 357 (2018) 237–244. <https://doi.org/10.1016/j.jnucmat.2018.07.006>.

49 358 [27] C.J. Ulmer, A.T. Motta, Characterization of faulted dislocation loops and cavities in ion
50 359 irradiated alloy 800H, *J. Nucl. Mater.* 498 (2018) 458–467.
51 360 <https://doi.org/10.1016/j.jnucmat.2017.11.012>.

53 361 [28] T. Yang, C. Lu, G. Velisa, K. Jin, P. Xiu, M.L. Crespillo, Y. Zhang, H. Bei, L. Wang,
54 362 Effect of alloying elements on defect evolution in Ni-20X binary alloys, *Acta Mater.* 151
55 363 (2018) 159–168. <https://doi.org/10.1016/j.actamat.2018.03.054>.

57 364 [29] P. Xiu, Y.N. Osetsky, L. Jiang, G. Velisa, Y. Tong, H. Bei, W.J. Weber, Y. Zhang, L.
58 365 Wang, Dislocation loop evolution and radiation hardening in nickel-based concentrated
59 366 solid solution alloys, *J. Nucl. Mater.* 538 (2020) 152247.

1
2
3
4 367 <https://doi.org/10.1016/j.jnucmat.2020.152247>.

5
6 368 [30] D. Chen, K. Murakami, K. Dohi, K. Nishida, Z. Li, N. Sekimura, The effects of loop size
7 369 on the unfauling of Frank loops in heavy ion irradiation, *J. Nucl. Mater.* 529 (2020)
8 370 151942. <https://doi.org/10.1016/j.jnucmat.2019.151942>.

9
10 371 [31] T. Chen, L. He, M.H. Cullison, C. Hay, J. Burns, Y. Wu, L. Tan, The correlation between
11 372 microstructure and nanoindentation property of neutron-irradiated austenitic alloy D9,
12 373 *Acta Mater.* 195 (2020) 433–445. <https://doi.org/10.1016/j.actamat.2020.05.020>.

13
14 374 [32] C. Chen, J. Zhang, J. Song, Comprehensive study of vacancy frank loop unfauling:
15 375 atomistic simulations and predictive model, *Acta Mater.* 208 (2021) 116745.
16 376 <https://doi.org/10.1016/j.actamat.2021.116745>.

17
18 377 [33] D.L. DOUGLASS, S.E. BRONISZ, Alpha Particle Irradiation Damage in ThO₂, *J. Am.*
19 378 *Ceram. Soc.* 54 (1971) 158–161. <https://doi.org/10.1111/j.1151-2916.1971.tb12245.x>.

20
21 379 [34] K. Bawane, X. Liu, T. Yao, M. Khafizov, A. French, J.M. Mann, L. Shao, J. Gan, D.H.
22 380 Hurley, L. He, TEM characterization of dislocation loops in proton irradiated single
23 381 crystal ThO₂, *J. Nucl. Mater.* 552 (2021) 152998.
24 382 <https://doi.org/10.1016/j.jnucmat.2021.152998>.

25
26 383 [35] L. He, T. Yao, K. Bawane, M. Jin, C. Jiang, M. Khafizov, X. Liu, W.-Y. Chen, J.M.
27 384 Mann, D.H. Hurley, J. Gan, Dislocation loop evolution in Kr-irradiated ThO₂, *J. Am.*
28 385 *Ceram. Soc.* submitted (2021).

29
30 386 [36] B. Yao, D.J. Edwards, R.J. Kurtz, TEM characterization of dislocation loops in irradiated
31 387 bcc Fe-based steels, *J. Nucl. Mater.* (2013). <https://doi.org/10.1016/j.jnucmat.2012.12.002>.

32
33 388 [37] C.M. Parish, K.G. Field, A.G. Certain, J.P. Wharry, Application of STEM characterization
34 389 for investigating radiation effects in BCC Fe-based alloys, *J. Mater. Res.* (2015).
35 390 <https://doi.org/10.1557/jmr.2015.32>.

36
37 391 [38] P. Xiu, H. Bei, Y. Zhang, L. Wang, K.G. Field, STEM Characterization of Dislocation
38 392 Loops in Irradiated FCC Alloys, *J. Nucl. Mater.* (2021).
39 393 <https://doi.org/10.1016/j.jnucmat.2020.152658>.

40
41 394 [39] K.G. Field, S.A. Briggs, X. Hu, Y. Yamamoto, R.H. Howard, K. Sridharan,
42 395 Heterogeneous dislocation loop formation near grain boundaries in a neutron-irradiated
43 396 commercial FeCrAl alloy, *J. Nucl. Mater.* (2017).
44 397 <https://doi.org/10.1016/j.jnucmat.2016.10.050>.

45
46 398 [40] K.G. Field, S.A. Briggs, K. Sridharan, Y. Yamamoto, R.H. Howard, Dislocation loop
47 399 formation in model FeCrAl alloys after neutron irradiation below 1 dpa, *J. Nucl. Mater.*
48 400 (2017). <https://doi.org/10.1016/j.jnucmat.2017.07.061>.

49
50 401 [41] Y. Zhu, C. Ophus, M.B. Toloczko, D.J. Edwards, Towards bend-contour-free dislocation
51 402 imaging via diffraction contrast STEM, *Ultramicroscopy.* (2018).
52 403 <https://doi.org/10.1016/j.ultramic.2018.06.001>.

53
54 404 [42] Y. Miyajima, M. Mitsuhashi, S. Hata, H. Nakashima, N. Tsuji, Quantification of internal
55 405 dislocation density using scanning transmission electron microscopy in ultrafine grained

1
2
3
4 406 pure aluminium fabricated by severe plastic deformation, *Mater. Sci. Eng. A.* (2010).
5 407 <https://doi.org/10.1016/j.msea.2010.09.058>.
6
7 408 [43] P.J. Phillips, M.C. Brandes, M.J. Mills, M. de Graef, Diffraction contrast STEM of
8 409 dislocations: Imaging and simulations, *Ultramicroscopy.* (2011).
9 410 <https://doi.org/10.1016/j.ultramic.2011.07.001>.
11
12 411 [44] C.B. Carter, D.B. Williams, *Transmission electron microscopy: Diffraction, imaging, and*
13 412 *spectrometry*, 2016. <https://doi.org/10.1007/978-3-319-26651-0>.
14
15 413 [45] W.J. Weber, Y. Zhang, Predicting damage production in monoatomic and multi-elemental
16 414 targets using stopping and range of ions in matter code: Challenges and recommendations,
17 415 *Curr. Opin. Solid State Mater. Sci.* (2019). <https://doi.org/10.1016/j.cossms.2019.06.001>.
18
19 416 [46] E.H. Lee, L.K. Mansur, M.H. Yoo, Spatial variation in void volume during charged
20 417 particle bombardment - the effects of injected interstitials, *J. Nucl. Mater.* (1979).
21 418 [https://doi.org/10.1016/0022-3115\(79\)90548-8](https://doi.org/10.1016/0022-3115(79)90548-8).
22
23 419 [47] F.A. Garner, Impact of the injected interstitial on the correlation of charged particle and
24 420 neutron-induced radiation damage, *J. Nucl. Mater.* (1983). [https://doi.org/10.1016/0022-](https://doi.org/10.1016/0022-3115(83)90023-5)
25 421 [3115\(83\)90023-5](https://doi.org/10.1016/0022-3115(83)90023-5).
26
27 422 [48] P.J. Phillips, M.J. Mills, M. De Graef, Systematic row and zone axis STEM defect image
28 423 simulations, *Philos. Mag.* (2011). <https://doi.org/10.1080/14786435.2010.547526>.
29
30 424 [49] P. Humble, M.H. Loretto, L.M. Clarebrough, The nature of defects in quenched nickel,
31 425 *Philos. Mag.* (1967). <https://doi.org/10.1080/14786436708227702>.
32
33 426 [50] D.J. Mazey, J.A. Hudson, Observation of large faulted interstitial loops in proton-
34 427 irradiated nickel, *J. Nucl. Mater.* (1970). [https://doi.org/10.1016/0022-3115\(70\)90177-7](https://doi.org/10.1016/0022-3115(70)90177-7).
35
36 428 [51] H.R. Brager, J.L. Straalsund, Defect development in neutron irradiated type 316 stainless
37 429 steel, *J. Nucl. Mater.* (1973). [https://doi.org/10.1016/0022-3115\(73\)90131-1](https://doi.org/10.1016/0022-3115(73)90131-1).
38
39 430 [52] C. Lu, T. Yang, L. Niu, Q. Peng, K. Jin, M.L. Crespillo, G. Velisa, H. Xue, F. Zhang, P.
40 431 Xiu, Y. Zhang, F. Gao, H. Bei, W.J. Weber, L. Wang, Interstitial migration behavior and
41 432 defect evolution in ion irradiated pure nickel and Ni-xFe binary alloys, *J. Nucl. Mater.*
42 433 (2018). <https://doi.org/10.1016/j.jnucmat.2018.07.006>.
43
44 434 [53] M.J. Whelan, P.B. Hirsch, Electron diffraction from crystals containing stacking faults: II,
45 435 *Philos. Mag.* (1957). <https://doi.org/10.1080/14786435708243208>.
46
47 436 [54] S. Plimpton, Fast Parallel Algorithms for Short-Range Molecular Dynamics, *J. Comput.*
48 437 *Phys.* 117 (1995) 1–19. <https://doi.org/10.1006/jcph.1995.1039>.
49
50 438 [55] V.I. Tseplyaev, S.V. Starikov, The atomistic simulation of pressure-induced phase
51 439 transition in uranium mononitride, *J. Nucl. Mater.* 480 (2016) 7–14.
52 440 <https://doi.org/10.1016/j.jnucmat.2016.07.048>.
53
54 441 [56] E.A. Kotomin, R.W. Grimes, Y. Mastrikov, N.J. Ashley, Atomic scale DFT simulations of
55 442 point defects in uranium nitride, *J. Phys. Condens. Matter.* 19 (2007) 106208.
56 443 <https://doi.org/10.1088/0953-8984/19/10/106208>.
57
58
59
60
61
62
63
64
65

1
2
3
4 444 [57] C. Dickerson, Y. Yang, T.R. Allen, Defects and microstructural evolution of proton
5 445 irradiated titanium carbide, *J. Nucl. Mater.* 424 (2012) 62–68.
6 446 <https://doi.org/10.1016/j.jnucmat.2012.02.005>.

8
9 447 [58] S. Agarwal, T. Koyanagi, A. Bhattacharya, L. Wang, Y. Katoh, X. Hu, M. Pagan, S.J.
10 448 Zinkle, Neutron irradiation-induced microstructure damage in ultra-high temperature
11 449 ceramic TiC, *Acta Mater.* 186 (2020) 1–10. <https://doi.org/10.1016/j.actamat.2019.12.022>.

13 450 [59] Y. Yang, C.A. Dickerson, H. Swoboda, B. Miller, T.R. Allen, Microstructure and
14 451 mechanical properties of proton irradiated zirconium carbide, *J. Nucl. Mater.* 378 (2008)
15 452 341–348. <https://doi.org/10.1016/j.jnucmat.2008.06.042>.

17 453 [60] F. Wang, X. Yan, T. Wang, Y. Wu, L. Shao, M. Nastasi, Y. Lu, B. Cui, Irradiation
18 454 damage in (Zr_{0.25}Ta_{0.25}Nb_{0.25}Ti_{0.25})C high-entropy carbide ceramics, *Acta Mater.* 195
19 455 (2020) 739–749. <https://doi.org/10.1016/j.actamat.2020.06.011>.

21 456 [61] J.P. Hirth, J. Lothe, T. Mura, *Theory of Dislocations* (2nd ed.), *J. Appl. Mech.* 50 (1983)
22 457 476–477. <https://doi.org/10.1115/1.3167075>.

24 458 [62] T. Kadoyoshi, H. Kaburaki, F. Shimizu, H. Kimizuka, S. Jitsukawa, J. Li, Molecular
25 459 dynamics study on the formation of stacking fault tetrahedra and unfauling of Frank loops
26 460 in fcc metals, *Acta Mater.* 55 (2007) 3073–3080.
27 461 <https://doi.org/10.1016/j.actamat.2007.01.010>.

30 462 [63] L.L. Snead, Y. Katoh, S. Kondo, Effects of fast neutron irradiation on zirconium carbide,
31 463 *J. Nucl. Mater.* 399 (2010) 200–207. <https://doi.org/10.1016/j.jnucmat.2010.01.020>.

33 464 [64] Y. Yang, W.-Y. Lo, C. Dickerson, T.R. Allen, Stoichiometry effect on the irradiation
34 465 response in the microstructure of zirconium carbides, *J. Nucl. Mater.* 454 (2014) 130–135.
35 466 <https://doi.org/10.1016/j.jnucmat.2014.07.071>.

37 467 [65] B.L. Eyre, R. Bullough, On the formation of interstitial loops in b.c.c. metals, *Philos.*
38 468 *Mag.* (1965). <https://doi.org/10.1080/14786436508224943>.

40 469 [66] J. Marian, B.D. Wirth, J.M. Perlado, Mechanism of Formation and Growth of [Formula
41 470 presented] Interstitial Loops in Ferritic Materials, *Phys. Rev. Lett.* (2002).
42 471 <https://doi.org/10.1103/PhysRevLett.88.255507>.

44 472 [67] K. Arakawa, M. Hatanaka, E. Kuramoto, K. Ono, H. Mori, Changes in the burgers vector
45 473 of perfect dislocation loops without contact with the external dislocations, *Phys. Rev. Lett.*
46 474 (2006). <https://doi.org/10.1103/PhysRevLett.96.125506>.

48 475 [68] S.L. Dudarev, R. Bullough, P.M. Derlet, Effect of the α - γ Phase transition on the stability
49 476 of dislocation loops in bcc iron, *Phys. Rev. Lett.* (2008).
50 477 <https://doi.org/10.1103/PhysRevLett.100.135503>.

52 478 [69] Z. Yao, M.L. Jenkins, M. Hernández-Mayoral, M.A. Kirk, The temperature dependence of
53 479 heavy-ion damage in iron: A microstructural transition at elevated temperatures, in:
54 480 *Philos. Mag.*, 2010. <https://doi.org/10.1080/14786430903430981>.

56 481 [70] K. Arakawa, T. Amino, H. Mori, Direct observation of the coalescence process between
57 482 nanoscale dislocation loops with different Burgers vectors, *Acta Mater.* (2011).

- 1
2
3
4 483 <https://doi.org/10.1016/j.actamat.2010.09.018>.
- 5
6 484 [71] J. Chen, N. Gao, P. Jung, T. Sauvage, A new mechanism of loop formation and
7 485 transformation in bcc iron without dislocation reaction, *J. Nucl. Mater.* (2013).
8 486 <https://doi.org/10.1016/j.jnucmat.2013.05.074>.
- 9
10 487 [72] H. Xu, R.E. Stoller, Y.N. Osetsky, D. Terentyev, Solving the puzzle of 100 Interstitial
11 488 Loop Formation in bcc Iron, *Phys. Rev. Lett.* (2013).
12 489 <https://doi.org/10.1103/PhysRevLett.110.265503>.
- 13
14
15 490 [73] Q. Peng, F. Meng, Y. Yang, C. Lu, H. Deng, L. Wang, S. De, F. Gao, Shockwave
16 491 generates < 100 > dislocation loops in bcc iron, *Nat. Commun.* (2018).
17 492 <https://doi.org/10.1038/s41467-018-07102-3>.
- 18
19 493 [74] D. Maestre, D. Häussler, A. Cremades, W. Jäger, J. Piqueras, Complex Defect Structure in
20 494 the Core of Sn-Doped In₂O₃ Nanorods and Its Relationship with a Dislocation-Driven
21 495 Growth Mechanism, *J. Phys. Chem. C*. 115 (2011) 18083–18087.
22 496 <https://doi.org/10.1021/jp204579u>.
- 23
24
25 497 [75] M.S. Elbakhshwan, Y. Miao, J.F. Stubbins, B.J. Heuser, Mechanical properties of UO₂
26 498 thin films under heavy ion irradiation using nanoindentation and finite element modeling,
27 499 *J. Nucl. Mater.* 479 (2016) 548–558. <https://doi.org/10.1016/j.jnucmat.2016.07.047>.
- 28
29 500 [76] J. Pakarinen, M. Khafizov, L. He, C. Wetteland, J. Gan, A.T. Nelson, D.H. Hurley, A. El-
30 501 Azab, T.R. Allen, Microstructure changes and thermal conductivity reduction in UO₂
31 502 following 3.9 MeV He²⁺ ion irradiation, *J. Nucl. Mater.* 454 (2014) 283–289.
32 503 <https://doi.org/10.1016/j.jnucmat.2014.07.053>.
- 33
34
35 504 [77] M. Khafizov, J. Pakarinen, L. He, D.H. Hurley, Impact of irradiation induced dislocation
36 505 loops on thermal conductivity in ceramics, *J. Am. Ceram. Soc.* 102 (2019) 7533–7542.
37 506 <https://doi.org/10.1111/jace.16616>.
- 38
39 507 [78] M. Khafizov, M.F. Riyad, Y. Wang, J. Pakarinen, L. He, T. Yao, A. El-Azab, D. Hurley,
40 508 Combining mesoscale thermal transport and x-ray diffraction measurements to
41 509 characterize early-stage evolution of irradiation-induced defects in ceramics, *Acta Mater.*
42 510 193 (2020) 61–70. <https://doi.org/10.1016/j.actamat.2020.04.018>.
- 43
44
45 511 [79] V.S. Chauhan, J. Pakarinen, T. Yao, L. He, D.H. Hurley, M. Khafizov, Indirect
46 512 characterization of point defects in proton irradiated ceria, *Materialia*. 15 (2021) 101019.
47 513 <https://doi.org/10.1016/j.mtla.2021.101019>.
- 48
49 514 [80] C.A. Dennett, Z. Hua, A. Khanolkar, T. Yao, P.K. Morgan, T.A. Prusnick, N. Poudel, A.
50 515 French, K. Gofryk, L. He, L. Shao, M. Khafizov, D.B. Turner, J.M. Mann, D.H. Hurley,
51 516 The influence of lattice defects, recombination, and clustering on thermal transport in
52 517 single crystal thorium dioxide, *APL Mater.* 8 (2020) 111103.
53 518 <https://doi.org/10.1063/5.0025384>.
- 54
55
56 519 [81] C.A. Dennett, W.R. Deskins, M. Khafizov, Z. Hua, A. Khanolkar, K. Bawane, L. Fu, J.M.
57 520 Mann, C.A. Marianetti, L. He, D.H. Hurley, A. El-Azab, An integrated experimental and
58 521 computational investigation of defect and microstructural effects on thermal transport in
59 522 thorium dioxide, *Acta Mater.* 213 (2021) 116934.

1
2
3
4
5
6
7
8
9
10
11
12
13
14
15
16
17
18
19
20
21
22
23
24
25
26
27
28
29
30
31
32
33
34
35
36
37
38
39
40
41
42
43
44
45
46
47
48
49
50
51
52
53
54
55
56
57
58
59
60
61
62
63
64
65

523
524
525

<https://doi.org/10.1016/j.actamat.2021.116934>.

Declaration of interests

The authors declare that they have no known competing financial interests or personal relationships that could have appeared to influence the work reported in this paper.

The authors declare the following financial interests/personal relationships which may be considered as potential competing interests: